



Co doping regulating electronic structure of Bi₂MoO₆ to construct dual active sites for photocatalytic nitrogen fixation

Chunming Yang, Yuanyuan Zhang, Feng Yue, Rui Du, Taoxia Ma, Yujie Bian, Ruqi Li, Li Guo*, Danjun Wang*, Feng Fu*

Yan'an Key Laboratory of Green Catalysis and Quality Improvement and Utilization of Low Rank Coal, College of Chemistry & Chemical Engineering, Yan'an University, Yan'an 716000, PR China



ARTICLE INFO

Keywords:

Co doping
Electronic structure regulation
Dual active sites
N≡N bond adsorption/activation

ABSTRACT

Although photocatalytic nitrogen reduction reaction (PNRR) is a green ammonia synthesis technology, it still encounters low adsorption/activation efficiency of N₂ and lack of reaction active sites. Element doping is an efficient strategy to regulate electronic structure of catalyst. Nevertheless, the mechanism of the effect of doping elements on the N₂ adsorption/activation, reaction active site and energy barriers is not well unraveled. Taking Co doped Bi₂MoO₆ (Co-Bi₂MoO₆) as a model photocatalyst, density functional theory (DFT) and experiment study were used to investigate the mechanism of Co doping on the PNRR performance over Bi₂MoO₆. DFT results reveal that Co doping regulates the electronic structure, activates Bi sites of Co-Bi₂MoO₆ and provides new Co active sites, thus constructing dual active sites for PNRR. Benefited from dual active sites for effectively adsorption/activation N₂, the as-fabricated 3% Co-Bi₂MoO₆ exhibit the maximum NH₃ generation rate of 95.5 μmol·g⁻¹·h⁻¹ without sacrificial agents, which is 7.2 times that of Bi₂MoO₆. Furthermore, the detail mechanism of N≡N bond adsorption/activation and hydrogenation reaction on Co-Bi₂MoO₆ was also proposed according to in-situ FTIR and DFT results. This study provides a promising strategy to design catalysts with dual active sites for PNRR, which is of great significance to the popularization of other material systems.

1. Introduction

Ammonia (NH₃) is a decisive component of the commercial synthesis of fertilizers, refrigerants and military applications [1]. Besides, NH₃ is an ideal hydrogen storage material, as it can easily condense into liquid for storage. Accordingly, it is assumed that NH₃ may play an important role in hydrogen economy and can be used as the power of fuel cells to provide a good strategy to deal with the energy crisis [2–4]. Currently, industrial ammonia is produced through Haber-Bosch process, which is conditioned by high-purity nitrogen (N₂) and hydrogen (H₂) streams under high pressure (15–25 MPa) and high temperature (400–500 °C), consuming a large amount of energy and capital [5]. These shortcomings have widely aroused interest in developing sustainable and environment-friendly strategies of ammonia synthesis to reach the ambitious carbon peak and carbon neutrality objectives [6,7].

Photocatalytic nitrogen reduction reaction (PNRR) is an attractive way to substitute for Haber-Bosch's production of NH₃ as it utilizes the inexhaustible solar and water to directly provide electrons and protons

for N₂ hydrogenation to NH₃, instead of supply high purity hydrogen [8,9]. The development of high-efficient PNRR catalysts has caused a range of research activities [10,11]. Unfortunately, most of currently developed photocatalytic materials still suffer from low adsorption/activation efficiency of N₂ and lack of reaction active sites, exhibiting limited conversion efficiencies for PNRR [12]. So far, numerous studies have been conducted to regulate the electronic structure of photocatalyst so as to optimize its nitrogen fixation performance [13]. Transitional metal element doping is widely used as an effective strategy to regulate the electronic structure to strengthen the N₂ adsorption/activation [14–17]. Xiong's group reported that Mo doping can efficiently enhance the N₂ adsorption/activation on the surface of W₁₈O₄₉ ultrathin nanowires, in which the coordinatively unsaturated metal atoms with oxygen defects serve as the sites for N₂ adsorption/activation [14]. Recently, Yin and co-works created new active sites on MoS₂ for the adsorption of N₂ and dissociation of nonpolar N≡N bond by Mn doping, in which the exposure of Mo edge sites is higher due to the formation of S vacancies [16]. Although the effect of element doping on regulation electronic structure

* Corresponding authors.

E-mail addresses: guoli20052017@163.com (L. Guo), wangdj761118@163.com (D. Wang), yadxfufeng@126.com (F. Fu).

and creation of defective-type active sites of photocatalyst has been well researched, the effect of doped element on inherent active sites, as well as act as new active sites on N₂ adsorption/activation and energy barriers over photocatalyst is not well unraveled.

In this work, taking Co doped Bi₂MoO₆ (Co-Bi₂MoO₆) as a model photocatalyst, density functional theory (DFT) was used to investigate the effect of Co-doping on partial density of states (DOS), differential charge density and energy barrier of Bi₂MoO₆. DFT results reveal that Co doping not only regulates the electronic structure, but also activates Bi sites of Co-Bi₂MoO₆ and provides new Co active sites, thus constructing dual active sites for PNRR. Under the guidance of DFT results, Co-Bi₂MoO₆ was synthesized by a facile solvothermal process. Ascribed to Co-doping regulated the electronic structure of Bi₂MoO₆ to construct dual active sites for effectively adsorption/activation N₂, the as-fabricated 3% Co-Bi₂MoO₆ achieved the maximum NH₃ generation rate of 95.5 μmol·g⁻¹·h⁻¹ under visible light irradiation without sacrificial agents, which is 7.2 times that of Bi₂MoO₆. Furthermore, the detail steps for N≡N bond adsorption/activation and hydrogenation reaction pathway on Co-Bi₂MoO₆ are depicted according to DFT and in-situ FTIR results. This study provides fresh insights into design catalysts with dual active sites for PNRR and reaffirms the versatility of subtle electronic structure modulation in tuning catalytic activity.

2. Experimental and computational section

2.1. Preparation of Bi₂MoO₆

Pure Bi₂MoO₆ was prepared by solvothermal method. Typically, under intense stirring, 1.94 g of Bi(NO₃)₃•5 H₂O (4 mmol) and 0.484 g of Na₂MoO₄•2 H₂O (2 mmol) were dissolved in a mixed solution of glycol (40 mL) and ethanol (10 mL) to obtain transparent liquid and transfer to a 65 mL autoclave lined with polytetrafluoroethylene for solvothermal reaction at 190 °C for 2 h. The yellow precipitation was then separated, washed with ethanol and deionized water for several times, and dried to obtain Bi₂MoO₆ product.

2.2. Preparation of Co-Bi₂MoO₆

The Co-Bi₂MoO₆ photocatalyst was prepared by hydrothermal method. In a typical process, 40 mL of 0.0005 mol·L⁻¹ CoCl₂·6 H₂O solution was taken into a 100 mL beaker, and 1 g of Bi₂MoO₆ was added to the solution, and stirred for 1 h. Finally, the homogeneous solution was transferred into a 65 mL Teflon-lined stainless steel autoclave and maintained at 160 °C for 5 h. The product was separated by centrifugation, washed with ethanol and deionized water for several times and then dried overnight. The obtained product was marked as 0.5% Co-Bi₂MoO₆. The change in CoCl₂·6 H₂O (0.001, 0.002, 0.003, 0.004, 0.006 mol·L⁻¹) concentration was used to create a series of samples for experimental optimization, which were referred to as X% Co-Bi₂MoO₆ (X = 0.5, 1, 2, 3, 4, 6, X means the mass ratio of CoCl₂·6 H₂O and Bi₂MoO₆).

2.3. Photocatalysis nitrogen reduction reaction

The photocatalytic activity of nitrogen fixation was evaluated under visible light. Generally, in a quartz reaction, add photocatalyst (100 mg) to ultrapure water (150 mL). Before irradiation, to eliminate dissolved oxygen, the suspension was rapidly agitated in the dark for 30 min and bubbled in high purity nitrogen. During irradiation, 7 mL of solution was taken out every 30 min, and then centrifuged at 11000 rpm for 5 min to remove photocatalyst for the following NH₃/NH₄⁺ concentration analysis.

2.4. Theoretical calculations

The DOS, differential charge density and energy barrier of Bi₂MoO₆

and Co-Bi₂MoO₆ were performed through the spin-polarized density functional theory (DFT) as implemented by the Vienna ab initio simulation package (VASP). Perdew-Burke-Ernzerhof (PBE) generalized gradient approximation (GGA) was used to describe the exchange-correlation energy functional. Projected augmented wave (PAW) pseudopotential was used for depicting the ion core and the periodic boundary condition. Spin polarization was also considered. A 2 × 1 supercell, three layers of pristine Bi₂MoO₆ (010) and Co-Bi₂MoO₆ (010) surface were chosen to construct the investigated models. Geometry optimizations, DOS, differential charge density and free energy were performed with a convergence threshold of 10⁻⁵ eV in energy and 0.05 eV/Å for the force. A vacuum of 15 Å along the z-direction was used, which was large enough to minimize the interactions between periodic images. The free energy of PNRR was calculated by using the equation:

$$\Delta G = E_{\text{surface+adsorbate}} - E_{\text{surface}} - E_{\text{adsorbate}} + \Delta E_{\text{ZPE}} - TS,$$

where G, E, ZPE and TS represent the free energy, total energy from DFT calculations, zero point energy and entropic contributions, respectively.

3. Results and discussion

3.1. DFT calculation for catalysts design

The key step in the PNRR process is known to be adsorption/activation of N₂ on catalyst surface. During the N₂ adsorption/activation process, the electrons on bonding orbital (highest occupied molecule orbital, HOMO, 2s_g) of N₂ interact with the d-orbital of catalyst active site to form the adsorption state. Then the d-orbital electrons of catalyst active site feedback to anti-bonding orbital (lowest unoccupied molecule orbital, LUMO, 1π_g) of the N₂ to activate the N≡N bond to form N₂ active state (-N₂), and then -N₂ reacts with the H⁺ and photo-generated electrons to form NH₃ (Fig. 1a). Hence, it is crucial that catalytic active site provide symmetric orbit matching with the anti-bonding orbital of the N₂.

Bismuth molybdate (Bi₂MoO₆) is a typical Aurivillius oxide, composed of a layered structure with alternate stacking of (Bi₂O₂)²⁺ sheets interleaved with [MoO₄]²⁻ layer [18]. The hybridization of Bi 6 s and O 2p orbit constitute its valence band (VB), Mo 4d (4d⁵) constitute its conduction band (CB) (Fig. 1b and c) [19,20]. Thermodynamic, the energy band structure of Bi₂MoO₆ meets the potential requirement of the PNRR [21]. Theoretically, the structure of Bi₂MoO₆ determines that Bi sites (Bi₂MoO₆-Bi) is responsible for N₂ molecule adsorption/activation other than Mo sites in the PNRR. Nevertheless, the Bi 6 s orbit is difficult to form adsorption states with the N₂ molecules. The Co atoms possesses ideal d-band electronic structure (3d⁷) that spatially matches the anti-bonding orbital of N₂ [22]. As shown in Fig. 1d, the high overlap of N, Bi, and Co peaks in the PDOS indicates that the Co-Bi₂MoO₆ is propitious to accept electrons from N₂ HOMO (2s_g) to form adsorbed state N₂, and then electrons transfer from the Co d-orbital to the anti-bonding orbital (LUMO, 1π_g) of N≡N to activate N₂. Furthermore, Co doping induces an impurity energy level near the top of Bi₂MoO₆ valence band, which is beneficial for electron excitation [23]. According to the differential charge density (Fig. 1e), it is clear that the electrons transfer from d-orbital Co sites (Co-Bi₂MoO₆-Co) to the anti-bonding orbital of adsorbed N₂. Therefore, the essence of the N₂ adsorption/activation on the surface of transition metal site (Co and Bi) is the “acceptance donation” of electrons, where the electron structure of d orbitals determines the energy barriers of PNRR.

The DFT calculations were further performed to gain insight into the effect of Co doping on N₂ adsorption/activation as well as reveal inherent mechanism of PNRR activity [24–26]. Fig. 2a exhibited the d-orbital DOS of Co-Bi₂MoO₆ and Bi₂MoO₆ to examine the influence of Co doping on the electronic structure. The d-band centers of Co-Bi₂MoO₆ and Bi₂MoO₆ are -3.1 and -2.7 eV, respectively. Co-doping resulted in shifting up d-band center of Bi₂MoO₆, which may be in favor of

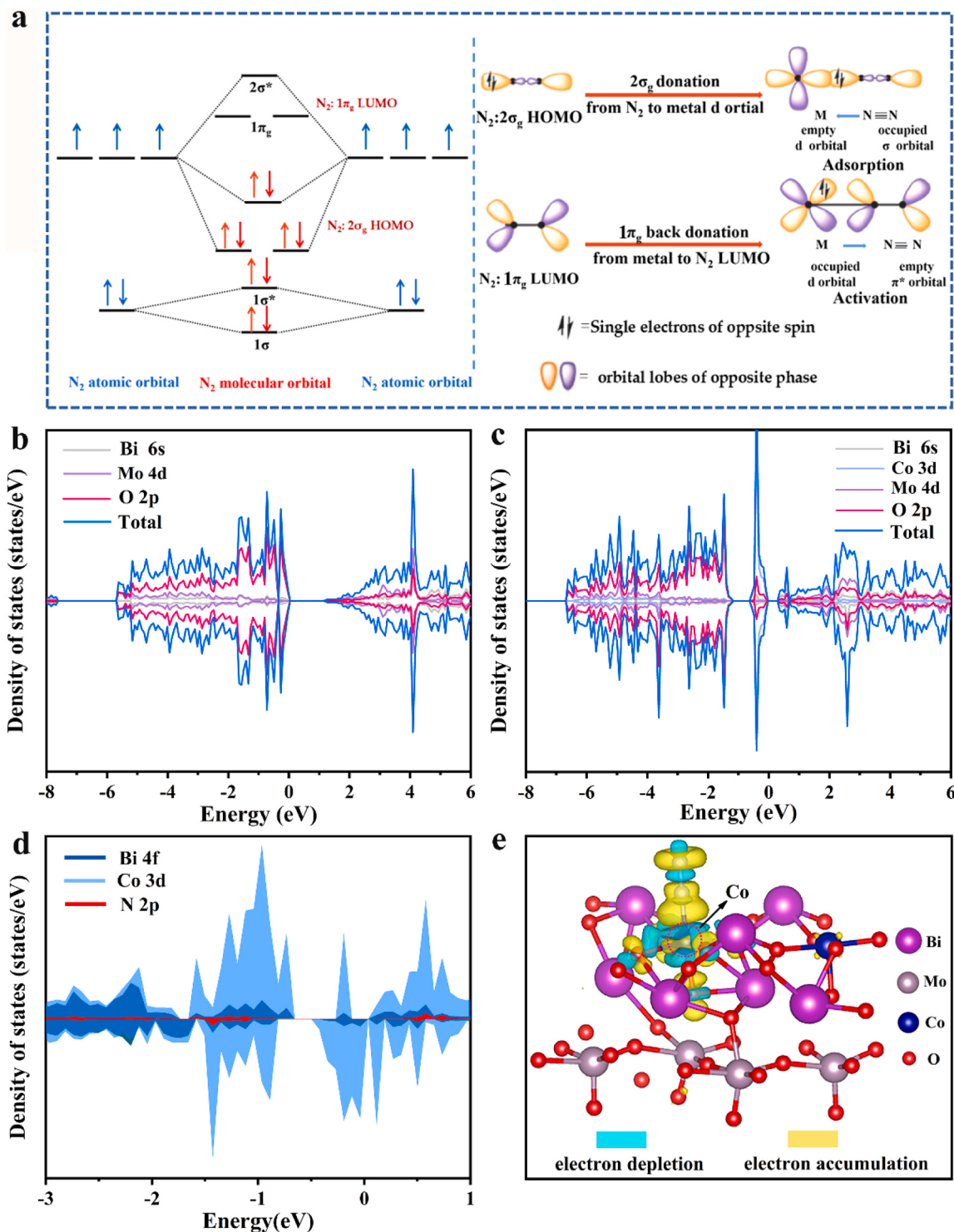


Fig. 1. (a) Schematic of $\text{N}\equiv\text{N}$ bond adsorption/activation process. The calculated DOS of (b) Bi_2MoO_6 , (c) $\text{Co}-\text{Bi}_2\text{MoO}_6$ and (d) $\text{Co}-\text{Bi}_2\text{MoO}_6$ with adsorbed N_2 . (e) Differential charge densities for $\text{Co}-\text{Bi}_2\text{MoO}_6$ -Co with adsorbed N_2 .

physical/chemical adsorption, activation and hydrogenation of N_2 molecule [25]. The Gibbs free energy of N_2 adsorption was calculated to identify the adsorption/activation ability of photocatalyst. The adsorption free energy of N_2 on Bi_2MoO_6 - Bi and on Bi sites in $\text{Co}-\text{Bi}_2\text{MoO}_6$ ($\text{Co}-\text{Bi}_2\text{MoO}_6$ - Bi) are -0.2 and -0.44 eV, respectively (Fig. 2b), indicating that Co doping can activate Bi sites ($\text{Co}-\text{Bi}_2\text{MoO}_6$ - Bi) and improve its adsorption/activation ability. Simultaneously, the adsorption free energy for N_2 on Co sites ($\text{Co}-\text{Bi}_2\text{MoO}_6$ - Co) is -0.59 eV, manifesting

that Co can be considered as the main adsorption sites during PNRR. Additionally, materials with enhanced adsorption performance correspond to weakened $\text{N}\equiv\text{N}$ triple bonds. As shown in Fig. 2b, the $\text{N}\equiv\text{N}$ lengths of $\text{Co}-\text{Bi}_2\text{MoO}_6$ - Co , $\text{Co}-\text{Bi}_2\text{MoO}_6$ - Bi are 1.132 and 1.118 Å, respectively, which exhibit significant elongations compared with that of Bi_2MoO_6 (1.117 Å).

To explore the entire reaction path of synthetic ammonia over Co_2MoO_6 , this process was determined by calculating the Gibbs free

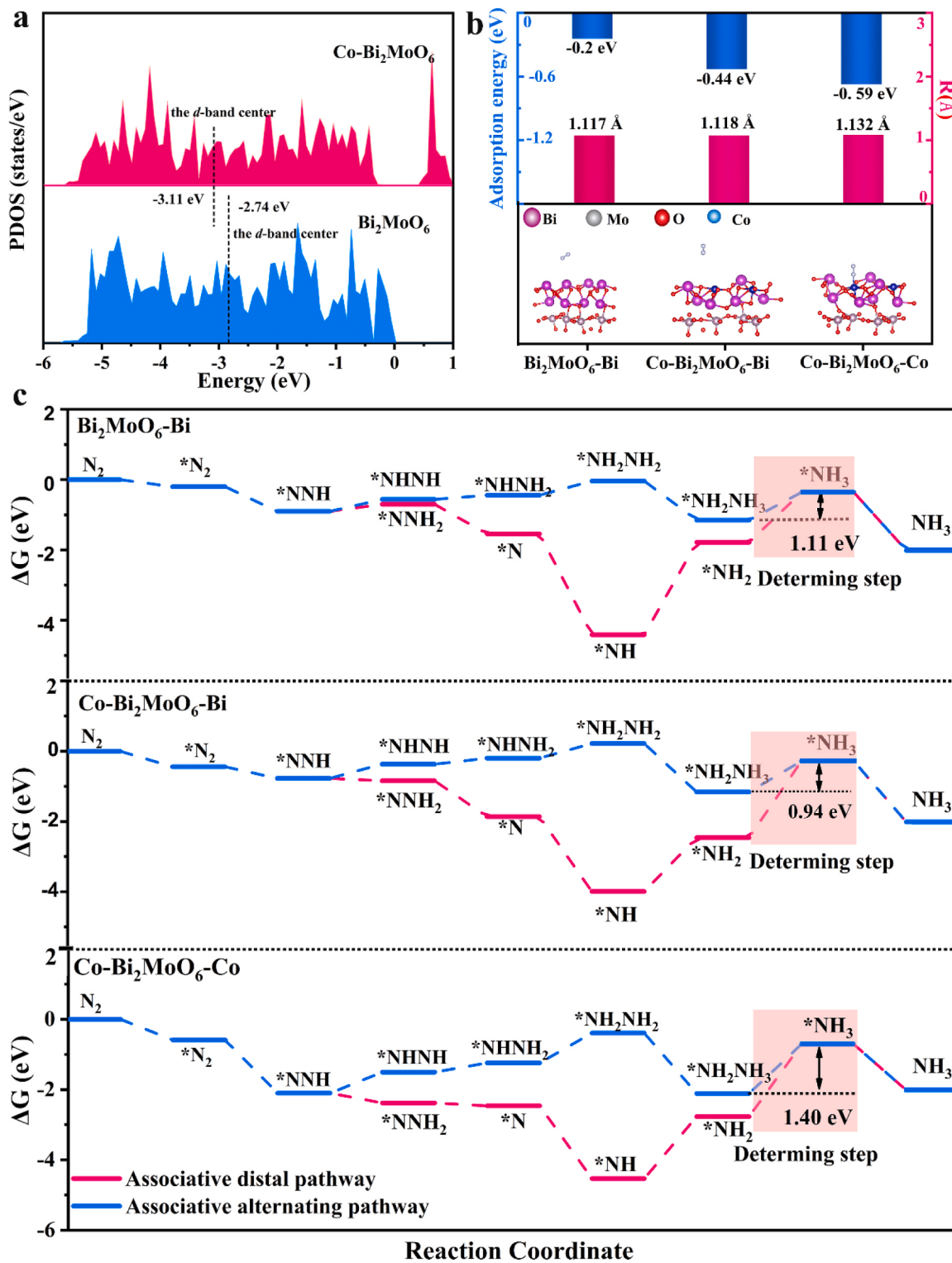


Fig. 2. (a) PDOS and d-band center calculation using the PBE method of Bi_2MoO_6 and $\text{Co-Bi}_2\text{MoO}_6$. (b) Calculated adsorption free energy and $\text{N}\equiv\text{N}$ lengths of N_2 on $\text{Bi}_2\text{MoO}_6\text{-Bi}$, $\text{Co-Bi}_2\text{MoO}_6\text{-Bi}$ and $\text{Co-Bi}_2\text{MoO}_6\text{-Co}$ sites. (c) Gibbs free energy diagram for N_2 reduction over Bi_2MoO_6 , $\text{Co-Bi}_2\text{MoO}_6\text{-Bi}$ and $\text{Co-Bi}_2\text{MoO}_6\text{-Co}$ sites.

energy (Fig. 2c and Fig. S1) [27]. Associative alternating pathway and associative distal pathway share the same initial hydrogenation step ($^*\text{N}_2 + \text{H}^+ + \text{e}^- \rightarrow ^*\text{N}-\text{NH}$), but the succeeding hydrogenation stages vary because of different processes [28]. Three kinds of active sites ($\text{Bi}_2\text{MoO}_6\text{-Bi}$, $\text{Co-Bi}_2\text{MoO}_6\text{-Bi}$, $\text{Co-Bi}_2\text{MoO}_6\text{-Co}$) follow the associative alternating pathway because the associative distal pathway exhibit the higher energy barriers. The rate-determining step ($^*\text{NH}_2\text{NH}_3 \rightarrow ^*\text{NH}_3$)

energy barriers of associative alternating pathway are 1.11, 0.94 and 1.4 eV, respectively. Although the rate-determining step energy barrier of $\text{Co-Bi}_2\text{MoO}_6\text{-Co}$ is relatively high, it possesses the strongest N_2 adsorption capacity among the three kinds of active sites. Since N_2 adsorption/activation is the key step of the PNRR, the $\text{Co-Bi}_2\text{MoO}_6\text{-Co}$ sites also act as active sites of PNRR as well as $\text{Co-Bi}_2\text{MoO}_6\text{-Bi}$ sites. Theoretically, Co doping regulates the electronic structure of Bi_2MoO_6 ,

activates the Co-Bi₂MoO₆-Bi sites, provides the new Co-Bi₂MoO₆-Co active sites, thus constructing dual active sites for PNRR.

3.2. Characterization of catalysts

Inspired by the theoretical results, we fabricated Bi₂MoO₆ and Co-Bi₂MoO₆ by a solvothermal method (Fig. S2). X-ray diffraction (XRD) was used to analyze the crystalline structures of Bi₂MoO₆ and Co-Bi₂MoO₆ with different Co contents. All diffraction peaks of Bi₂MoO₆ conformed to the orthorhombic Bi₂MoO₆ structure (JCPDS No.76–2388) (Fig. 3a). Additionally, the peak intensity of (131) and (002) planes in Bi₂MoO₆ decreased with the increase of cobalt content and no new peaks were detected in the XRD patterns of Co-Bi₂MoO₆. The enlarged XRD patterns in the range of 25–35° indicated the characteristic peaks (131) and (002) gradually shift to the higher angle. Since the atomic radius of Co was smaller than that of Bi, it was certain that the Bi atoms in the main crystal were partially replaced by Co atoms (Fig. 3b) [29,30].

X-ray photoelectron spectroscopy (XPS) was employed to reveal the chemical valence of Bi₂MoO₆ and 3% Co-Bi₂MoO₆ (Fig. 3c-f and Fig. S3). As shown in Fig. 3c, the binding energy of Bi appeared at 159.12 and 164.43 eV in 3% Co-Bi₂MoO₆ could be attributed to Bi 4 f_{7/2} and Bi 4 f_{5/2} respectively, indicating that Bi exists in the form of Bi³⁺ [31]. The binding energy of Mo 3d in 3% Co-Bi₂MoO₆ (232.39 and 235.53 eV) was in accordance with Mo 3d_{3/2} and Mo 3d_{5/2} of Mo⁶⁺ (Fig. 3d) [32]. The binding energy of Bi 4 f and Mo 3d peaks is slightly higher than that of Bi₂MoO₆, indicating that the electron cloud density around Bi and Mo is decreased due to the doping of Co²⁺. Considering that Co (1.7) has a bigger Alley-Luo Zhou electronegativity than Bi (1.67) and Mo (1.30), the substitution of Bi³⁺ by Co²⁺ may cause bonding electrons to accumulate on Co²⁺, decreasing the electron cloud density of Bi and Mo elements and increasing the binding energy. The O 1 s of Bi₂MoO₆ and Co-Bi₂MoO₆ exhibited two characteristic peaks, the binding energy of 529.82 and 530.7 eV was attributed to lattice oxygen (Bi-O, Mo-O) and adsorbed oxygen, respectively (Fig. 3e) [33,34]. For 3% Co-Bi₂MoO₆,

two characteristic peaks of Co 2p at 780.99 and 805.33 eV belong to Co 2p_{3/2} and Co 2p_{1/2} indicate the chemical state of Co²⁺ (Fig. 3f) [35].

The morphology of Bi₂MoO₆ and 3% Co-Bi₂MoO₆ was investigated using scanning electron microscope (SEM) and transmission electron microscope (TEM), as shown in Fig. S4 and Fig. 4. Both Bi₂MoO₆ and Co-Bi₂MoO₆ exhibited spherical structure with an average diameter of about 3–5 μm (Fig. 4a and d). Furthermore, the HRTEM image clearly displayed lattice stripes of Bi₂MoO₆ and 3% Co-Bi₂MoO₆ at (131) plane raised from 0.315 to 0.335 nm (Fig. 4c and f) [36]. The energy dispersive X-ray (EDX) mapping further proved that 3% Co-Bi₂MoO₆ was composed of Bi, Mo, O and Co elements (Fig. 4g).

3.3. Nitrogen fixation performance

Pure water and pure nitrogen were employed as feedstocks, without adding sacrificial reagent, the PNRR activity of Bi₂MoO₆ and Co-Bi₂MoO₆ was carried out under visible light ($\lambda > 420$ nm) and simulated sunlight irradiation, respectively. The generated ammonia (NH₃/NH₄⁺) was measured by Nessler's reagent method (Fig. S5). As shown in Fig. 5a, the NH₃/NH₄⁺ yield of Bi₂MoO₆ was approximately 10 μmol·g⁻¹·h⁻¹ under visible light. After Co was doped into Bi₂MoO₆, the PNRR activity was significantly improved. Meanwhile, it manifested a volcano-type activity in NH₃/NH₄⁺ yield, which was a function of Co content. Particularly, the 3% Co-Bi₂MoO₆ exhibited the highest NH₃/NH₄⁺ yield rate of up to 95.5 μmol·g⁻¹·h⁻¹, which was 7.2-fold higher than that of the Bi₂MoO₆ and was prominent in the reported literatures (Table S1). While further increasing the Co doping content, the PNRR activity of Co-Bi₂MoO₆ decreased due to the excessive Co doping leading to lower separation efficiency of photo-generated e⁻/h⁺ pairs. The as-produced ammonia source was testified by the isotope labeling experiment. ¹⁵N₂ and ¹⁴N₂ with high purity were used as feed gases. As shown in ¹H nuclear magnetic resonance spectroscopy (NMR) (Fig. 5b), when ¹⁴N₂ was introduced into the PNRR experiment, the split triplet state of the ¹⁴NH₄⁺ signal appeared. Nevertheless, two symmetrical splitting

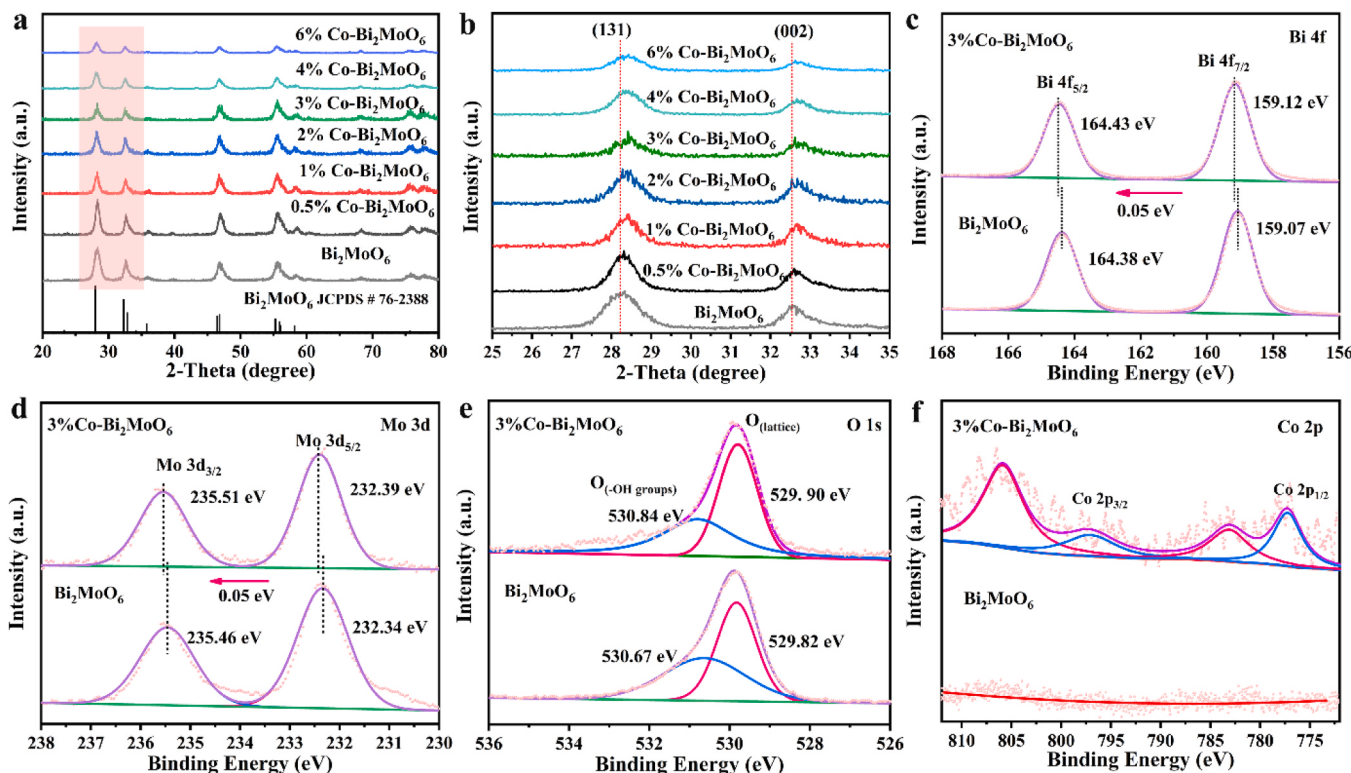


Fig. 3. (a) XRD patterns of Bi₂MoO₆ and Co-Bi₂MoO₆. (b) Magnified patterns of (131) and (002) crystal plane of Bi₂MoO₆ and Co-Bi₂MoO₆ in the range of 25–35° and XPS spectra of (c) Bi 4f, (d) Mo 3d, (e) O 1s and (f) Co 2p for Bi₂MoO₆ and 3% Co-Bi₂MoO₆.

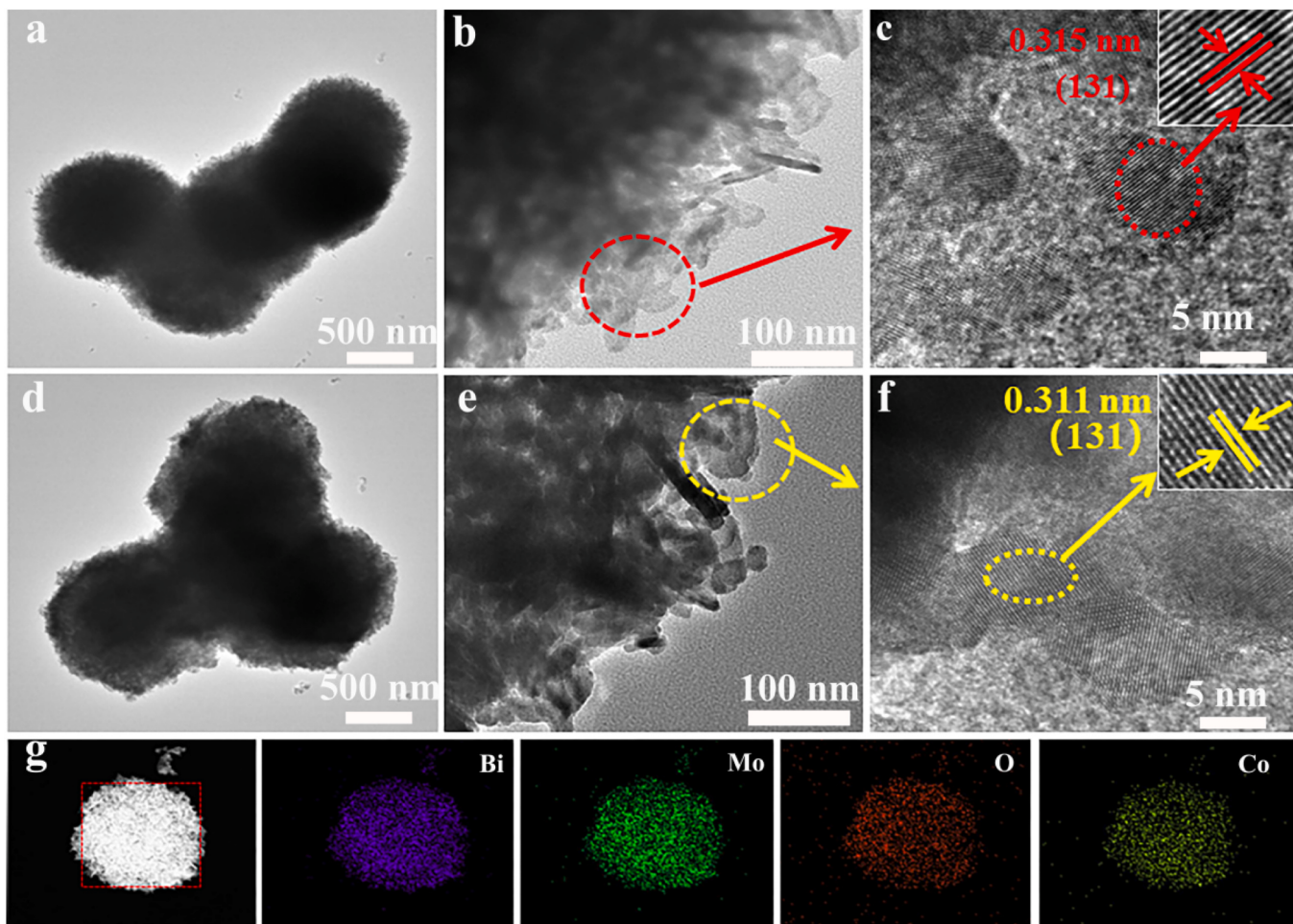


Fig. 4. TEM images of (a-b) Bi_2MoO_6 , (d-e) 3% Co- Bi_2MoO_6 . (c, f) HRTEM images of Bi_2MoO_6 and 3% Co- Bi_2MoO_6 , respectively. (g) EDX-mapping containing Bi, Mo, O and Co elements.

peaks of $^{15}\text{NH}_4^+$ were obviously observed when used $^{15}\text{N}_2$, which may be relevant to the coupling between ^1H resonance and ^{15}N , and in good agreement with the standard ^{15}N signal [37]. These results strongly verified that the ammonia produced indeed originated from N_2 fixation reaction rather than other nitrogen impurities.

To evaluate the light utilization efficiency, the apparent quantum efficiency (AQE) of 3% Co- Bi_2MoO_6 irradiated by monochromatic light was also measured (Fig. 5c). The AQE of 3% Co- Bi_2MoO_6 is in accordance with UV-vis diffuse reflectance spectrum, which indicates that it had high utilization efficiency of incident light. Specifically, with the increase of monochromatic light wavelength (i.e., 365, 380, 400, 420, 450, 500 and 550 nm), AQE decreased (1.009%, 0.806%, 0.561%, 0.224%, 0.172%, 0.074% and 0.02%). Moreover, the controllable experiments revealed that 3% Co- Bi_2MoO_6 do not produce ammonia under Ar atmosphere or dark conditions, indicating that the $\text{NH}_3/\text{NH}_4^+$ produced by 3% Co- Bi_2MoO_6 in pure H_2O under N_2 atmosphere and light irradiation was the result of PNRR (Fig. 5d). The ion chromatography (IC) was also used for detecting the produced $\text{NH}_3/\text{NH}_4^+$, which was quantified to be about $103 \mu\text{mol} \cdot \text{g}_{\text{cat}}^{-1} \cdot \text{h}^{-1}$ (Fig. S6), matching the value determined by the Nessler's reagent method.

It should be noted that there were negligible by-products N_2H_4 and NO_3^- , indicating the high selectivity of $\text{NH}_3/\text{NH}_4^+$ (Fig. S7 and S8) [38]. Furthermore, the cycling experiments indicated that 3% Co- Bi_2MoO_6 has a relatively stable ammonia production rate during 5 cycles (Fig. S9). Moreover, the crystal structure of Co- Bi_2MoO_6 after PNRR was investigated, as shown in Fig. S10. The XRD revealed that no phase significant difference occurred for 3% Co- Bi_2MoO_6 before and after

illumination, further confirming its great PNRR stability.

3.4. Nitrogen fixation mechanism investigation

To further investigate the mechanism for the enhanced PNRR activity of 3% Co- Bi_2MoO_6 , the energy band structure and the carrier dynamics were systematically analyzed. The UV-vis diffuse reflectance absorption spectra (UV-Vis DRS) indicates that the absorption threshold of Co- Bi_2MoO_6 presented red-shift, indicating that Co doping broadens the absorption range of Bi_2MoO_6 (Fig. 6a). On the basis of the Tauc curves by Kubelka-Munk equation, the calculated band gap (E_g) of Bi_2MoO_6 and 3% Co- Bi_2MoO_6 were determined to be 2.52 and 2.39 eV, respectively (insert picture in Fig. 6a). The conduction band minimum (CBM) of Bi_2MoO_6 and 3% Co- Bi_2MoO_6 was estimated according to Mott-Schottky curve. It indicated that the curve slopes of Bi_2MoO_6 and 3% Co- Bi_2MoO_6 were both positive, confirming both of them were n-type semiconductors, and the flat band potentials (E_{fb} vs. NHE) are -0.36 and -0.43 V vs NHE, respectively (Fig. 6b). It is well-accepted that the conduction band potential of n-type is closed to its flat band potential [39]. Thus, the CBM values of Bi_2MoO_6 and 3% Co- Bi_2MoO_6 were estimated to be -0.36 and -0.43 V, respectively. According to the empirical formula ($E_g = E_{\text{VBM}} - E_{\text{CBM}}$), the valence band maximum (VBM) values of Bi_2MoO_6 and 3% Co- Bi_2MoO_6 were calculated to be 2.16 and 1.96 V vs NHE, respectively, which were consistent with the valence band XPS results (Fig. 6c). Fig. 6d depicted the band gap structure of Bi_2MoO_6 and 3% Co- Bi_2MoO_6 and the standard reduction potential of some chemicals. It should be noted that the potentials of the

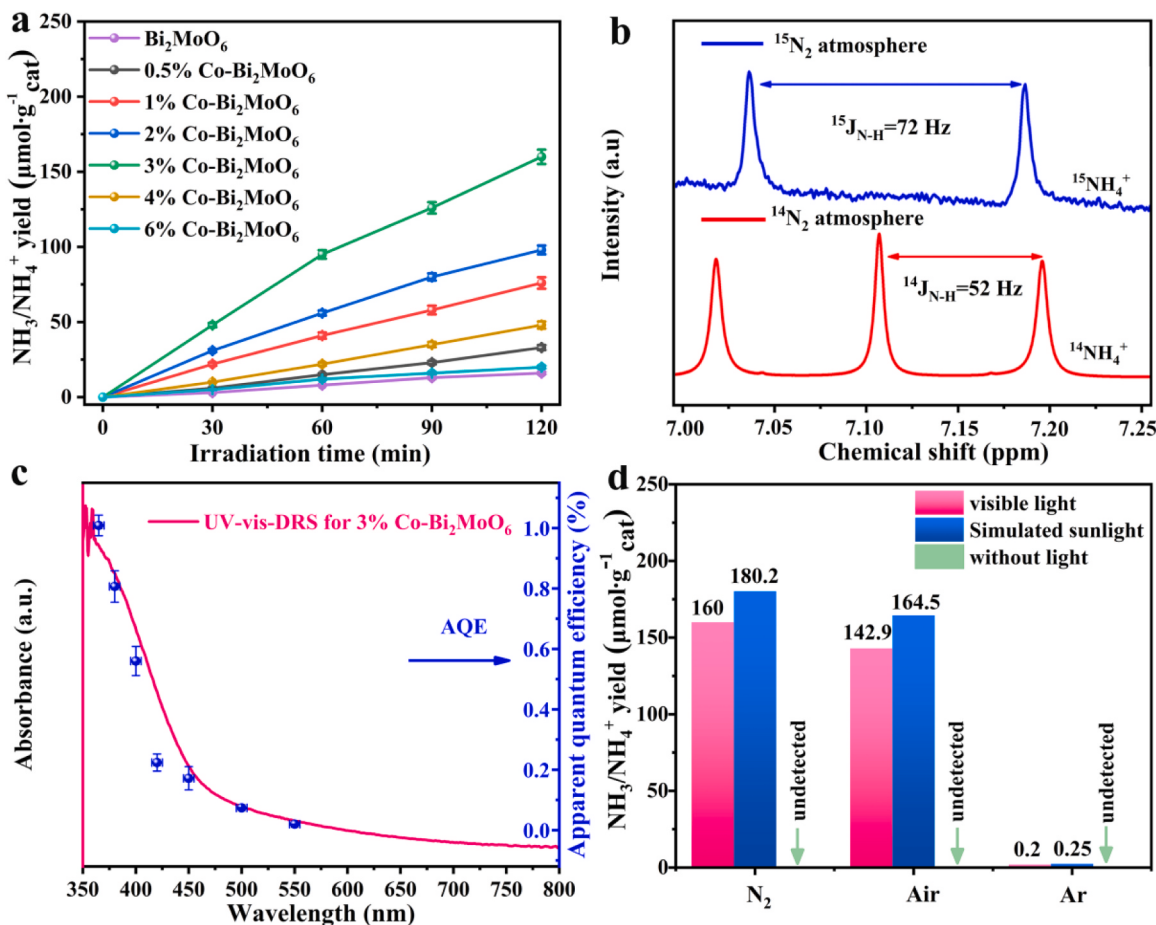


Fig. 5. (a) Photocatalytic N_2 fixation performance of Bi_2MoO_6 and Co-Bi₂MoO₆ under visible light. (b) ¹H NMR spectrum for produced NH_4^+ using N_2 (¹⁵ N_2 and ¹⁴ N_2) and water as feedstock. (c) Calculated AQEs for PNRR over 3% Co-Bi₂MoO₆ under monochromatic light irradiation. (d) Comparison of 3% Co-Bi₂MoO₆ with different nitrogen sources under visible light and simulated sunlight, respectively.

CBM and the VBM can drive the PNRR half-reaction and the water oxidation half-reaction, respectively ($E_{\text{CBM}} < \varphi\text{N}_2$, $\text{H}^+/\text{NH}_3 < \varphi\text{N}_2$ and $E_{\text{VBM}} > \varphi\text{O}_2$, $\text{H}^+/\text{H}_2\text{O}$) [40]. Therefore, Co-Bi₂MoO₆ had more negative conduction band and excellent nitrogen reduction performance, which is conducive to improve PNRR activity.

The electrochemical performance of the Bi_2MoO_6 and 3% Co-Bi₂MoO₆ was studied by transient photocurrent and electrochemical impedance spectra (EIS), which provided the information of charge separation and transfer dynamics of photocatalyst [41]. As shown in Fig. 7a and Fig. S11, Co doping can obviously increase the photocurrent density of Bi_2MoO_6 , implying that the Co doping can improve the separation of carriers efficiency. Nevertheless, the excessive doped Co may act as the recombination centre which lead to the recombination of photogeneration e^-/h^+ . The charge transfer resistance at the FTO/catalyst (R_1) and the catalyst/electrolyte interface (R_2) was calculated according to the Nyquist plots [42]. As shown in Fig. 7b, after Co doping, the R_2 was decreased from $3555\ \Omega$ to $1391\ \Omega$, indicating that Co-Bi₂MoO₆ had lower charge-transfer resistance. These results suggested that 3% Co-Bi₂MoO₆ possess better charge separation efficiency than Bi_2MoO_6 , implying its higher carrier transfer dynamics at the photocatalyst/solution interface. The photoluminescence (PL) intensity of 3% Co-Bi₂MoO₆ was lower than Bi_2MoO_6 , indicating that Co doping can hinder the recombination of photogenerated carries (Fig. 7c). The decay dynamics was also observed from time-resolved fluorescence decay spectroscopy (Fig. 7d). It revealed that carrier lifetime of 3% Co-Bi₂MoO₆ (2.78 ns) was longer than that of Bi_2MoO_6 (2.16 ns), implying that carrier migration and transportation had been improved.

The nitrogen temperature-programmed desorption (N₂-TPD)

indicated that physisorption/chemisorption peaks of 3% Co-Bi₂MoO₆ were stronger than those of Bi_2MoO_6 , reflecting an improvement in 3% Co-Bi₂MoO₆ adsorption and activation capacity for N_2 (Fig. 8a), thus significantly improving the activation of N_2 molecule and PNRR performance [43]. Furthermore, in-situ FTIR was employed to further investigate the progress of adsorption/activation and hydrogenation on the surface of 3% Co-Bi₂MoO₆ (Fig. 8b). During the PNRR process, a number of oscillation bands can be easily distinguished after the dark adsorption equilibrium. The peak I at 3385 cm^{-1} was related to N-H stretching mode. The characteristic absorption peaks of NH_4^+ and NH_3 were assigned to the peak II (2882 cm^{-1}), peak V (1403 cm^{-1}) and peak IV (1557 cm^{-1}), respectively [44,45]. The characteristic absorption peak of the ${}^{\bullet}\text{N}_2$ was corresponded to the peak III located at 1649 cm^{-1} [46]. Additionally, the intensity of peaks II and V increased with the extension of irradiation time. It is worth noting that two characteristic vibrations of hydrazine were not observed at 1290 and 1129 cm^{-1} [46].

Furthermore, the formation of superoxide radicals ($\bullet\text{O}_2$) was investigated by in-situ ESR technique, which can indirectly testify the oxidation half-reaction in the process of PNRR ($\text{H}_2\text{O} + \text{h}^+ \rightarrow \text{H}^+ + \text{O}_2 + e^-$). As shown in Fig. 9, the $\bullet\text{O}_2$ produced by 3% Co-Bi₂MoO₆ in the atmosphere of Ar, air and N_2 were monitored and studied with dimethylpyridine nitrogen oxide (DMPO) as the scavenger. The typical EPR signal of DMPO- $\bullet\text{O}_2$ of 3% Co-Bi₂MoO₆ gradually increased, proving the production of O_2 and the formation of $\bullet\text{O}_2$ due to the capturing the conduction band electrons of the catalyst by oxygen molecules ($\text{O}_2 + e^- \rightarrow \bullet\text{O}_2$). Under the visible light irradiation, the concentration of DMPO- $\bullet\text{O}_2$ adduct produced by 3% Co-Bi₂MoO₆ was much higher than that of Bi_2MoO_6 , which indicates that 3% Co-Bi₂MoO₆ produced more active

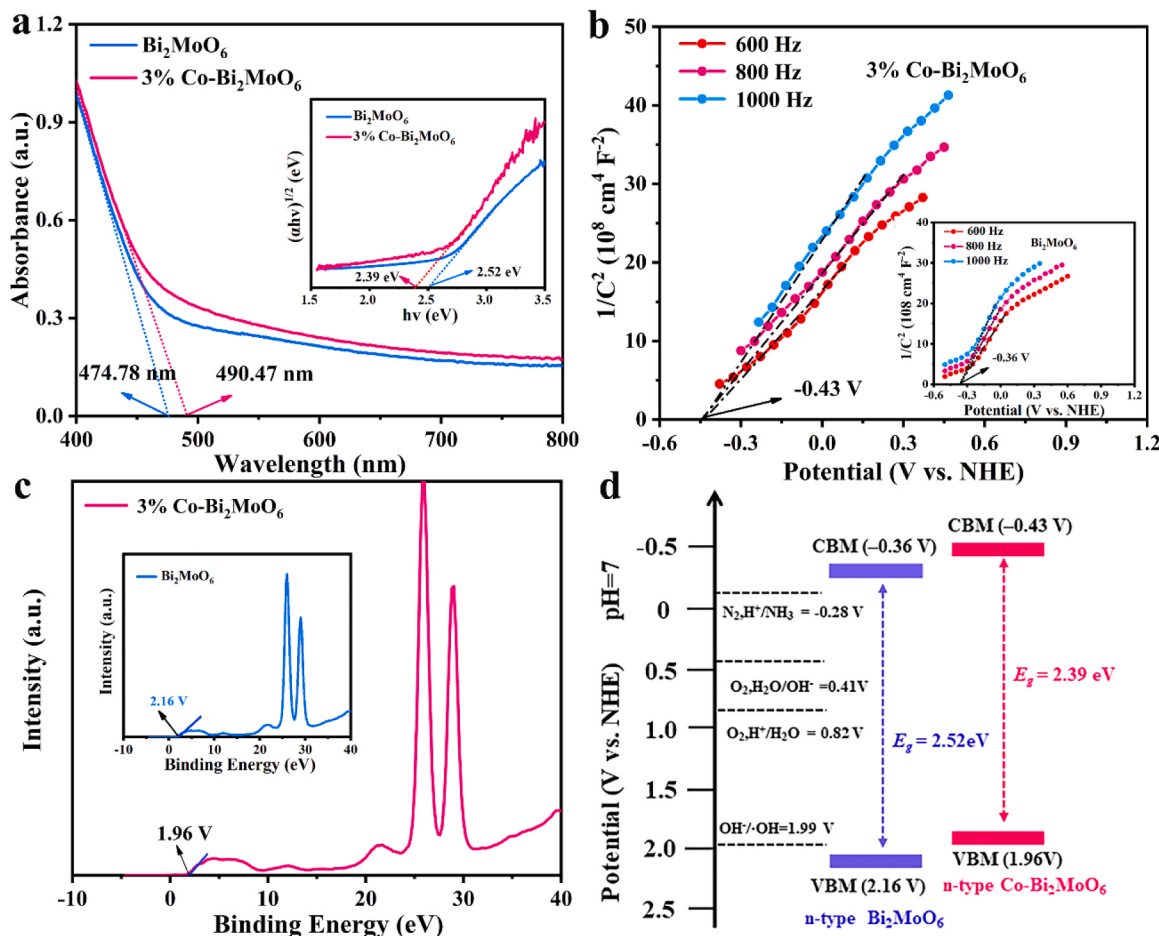


Fig. 6. (a) UV-vis DRS spectra of Bi₂MoO₆ and 3% Co-Bi₂MoO₆ (the inset shows corresponding Tauc plots [$(F(R)\hbar\nu)^{1/2}$ versus photon energy ($\hbar\nu$)]). (b) Mott-Schottky plots of Bi₂MoO₆ (inset) and 3%-Co-Bi₂MoO₆ under different alternating current potential frequency. (c) Valence band XPS spectrum of Bi₂MoO₆ (inset) and 3%Co-Bi₂MoO₆. (d) Schematic illustration of the band structure for Bi₂MoO₆ and 3% Co-Bi₂MoO₆.

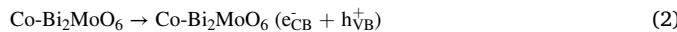
radicals (Fig. S12).

Fig. 10 shows a schematic of the PNRR mechanism on Co-Bi₂MoO₆ with dual active sites using N₂ and H₂O as feedstock without sacrifice agents (Eq.1), which mainly involves the following steps: i) Under light irradiation, electrons are excited from the VBM of Co-Bi₂MoO₆ to CBM, h⁺ are generated in VBM. The produced e⁻/h⁺ pairs transferred to the surface of the photocatalyst, where the photocatalytic N₂ fixation occurs (Eq.2). ii) The adsorption state N₂ (*N₂) was formed on Co and Bi dual active sites via the interaction with N₂ (2δ_g, HOMO) and unoccupied orbitals of Co-Bi₂MoO₆ (Eq.3). iii) The orbital electrons of Co and Bi active sites feedback to anti-bonding orbital (1π_g, LUMO) of N₂ to activate the N≡N bond, achieving the N₂ active state (-N₂) (Eq.4). iv) H₂O is oxidized by the h_{VB}⁺ to produce O₂ and release H⁺ and e⁻ (Eq.5). Simultaneously, O₂ capture e_{CB}⁻ to produce O₂^{·-}, which was testified by In-situ ESR (Fig. 9) (Eq. 6). v) The-N₂ reacts with the H⁺ and e_{CB}⁻ to form NH₃ (Eq. 7).

Overall reaction:

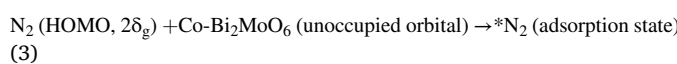


Step 1: Carrier generation and spatial separation.

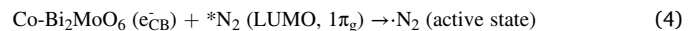


Step 2: N₂ adsorption/activation on Co and Bi active sites.

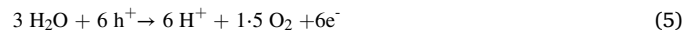
N₂ adsorption:



N≡N bond activation:



Step 3: Water oxidation half-reaction to produce O₂ and release H⁺ and e⁻



Step 4: Photocatalytic NRR half-reaction to produce NH₃.



4. Conclusion

In summary, based on the DFT calculation, Co doping regulates the electronic structure of Bi₂MoO₆, activates Bi sites of Co doped Bi₂MoO₆ (Co-Bi₂MoO₆) and provides new Co active sites, thus constructing dual active sites for PNRR. We successfully construct Co-Bi₂MoO₆ photocatalyst with dual active sites to investigate the effect of Co doping on the adsorption/activation and hydrogenation reaction. The as-prepared 3% Co-Bi₂MoO₆ exhibit the maximum NH₃ generation rate of 95.5 μmol·g⁻¹·h⁻¹ without sacrificial agents, which is 7.2 times that of Bi₂MoO₆. These performance enhancements can be attributed to the following: i) Co doping induces an impurity energy level near the top of Bi₂MoO₆ valence band, which is beneficial for accelerating the

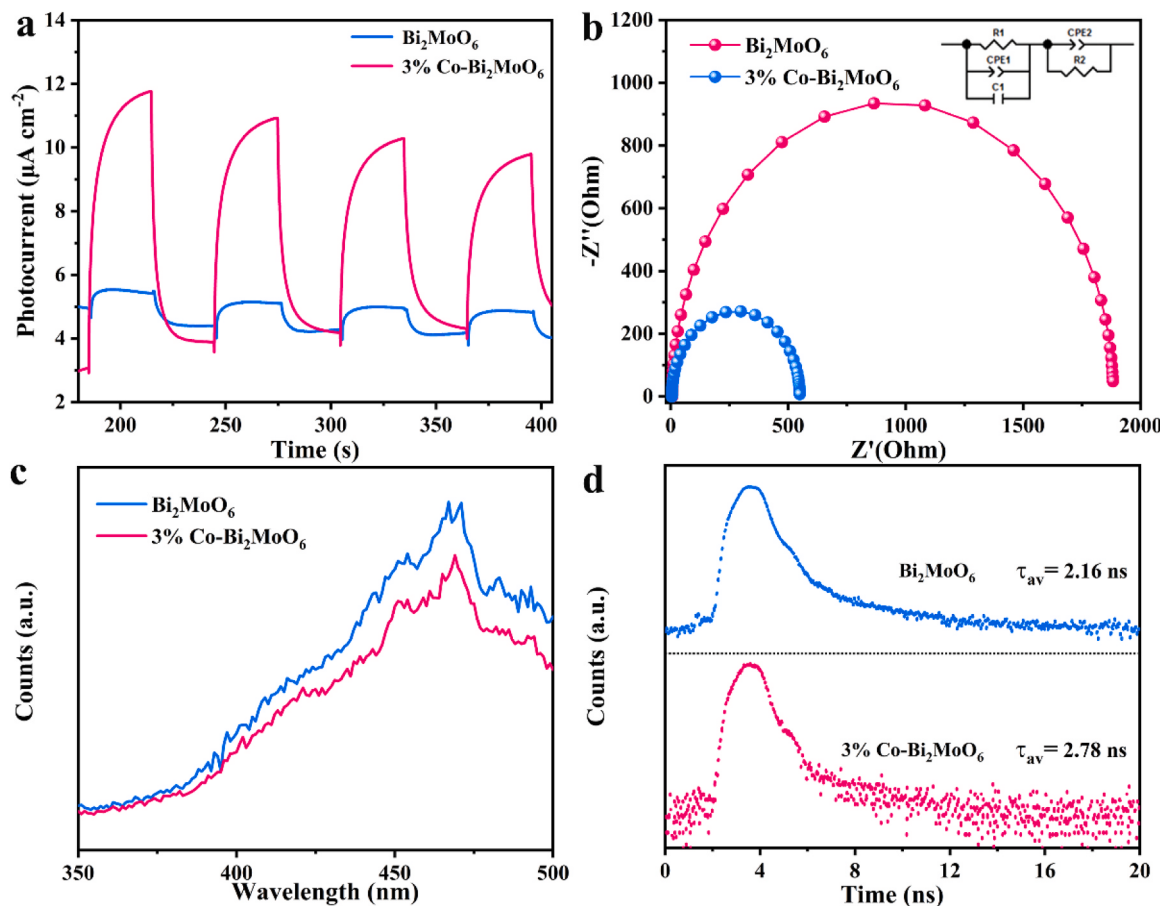


Fig. 7. (a) Photocurrent response plots, (b) Nyquist plots, (c) The room temperature PL spectra ($\lambda_{\text{excitation}} = 270 \text{ nm}$) and (d) Time-resolved fluorescence decay spectra of Bi_2MoO_6 and 3% $\text{Co}-\text{Bi}_2\text{MoO}_6$.

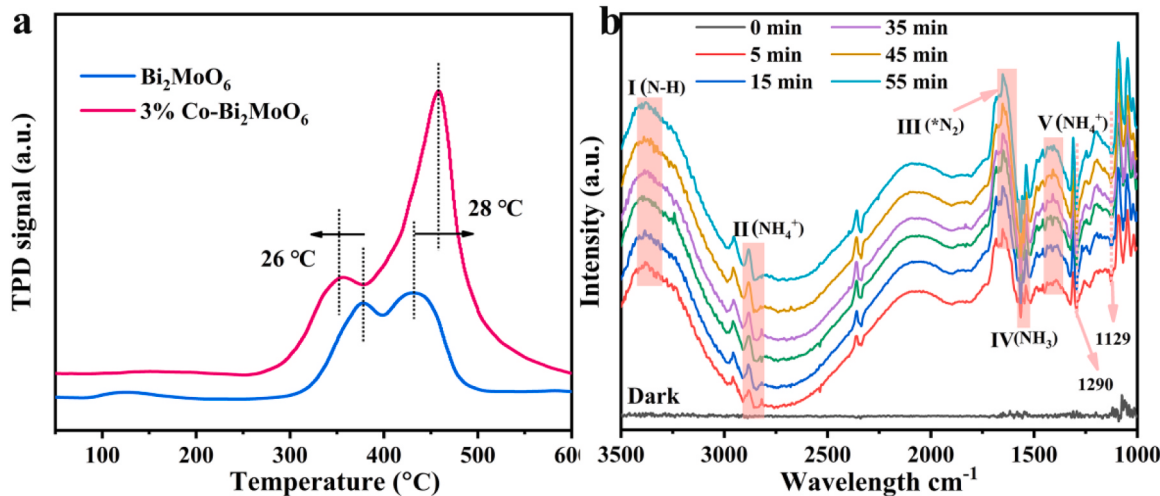


Fig. 8. (a) N₂-TPD profiles of the as-prepared Bi_2MoO_6 and 3% $\text{Co}-\text{Bi}_2\text{MoO}_6$. (b) In-situ FTIR spectra of N₂ fixation on 3% $\text{Co}-\text{Bi}_2\text{MoO}_6$ for up to 55 min's photoirradiation.

separation/transformation dynamics of carrier as well as enhancing the redox ability of Bi_2MoO_6 . ii) Co doping regulates the electronic structure of Bi_2MoO_6 , activates the $\text{Co}-\text{Bi}_2\text{MoO}_6$ -Bi sites, provides the new $\text{Co}-\text{Bi}_2\text{MoO}_6$ -Co active sites, thus constructing dual active sites for PNRR. Finally, the boosted mechanism of PNRR on $\text{Co}-\text{Bi}_2\text{MoO}_6$ with dual active sites was also proposed according to in-situ FTIR and DFT results. The present study provides a promising reference for combination of

DFT and experiment to design and construct high-efficiency nitrogen fixation photocatalysts.

CRediT authorship contribution statement

Chunming Yang: Methodology, Data curation, Writing. **Yuanyuan Zhang:** Methodology, Data curation. **Feng Yue:** Methodology, Data

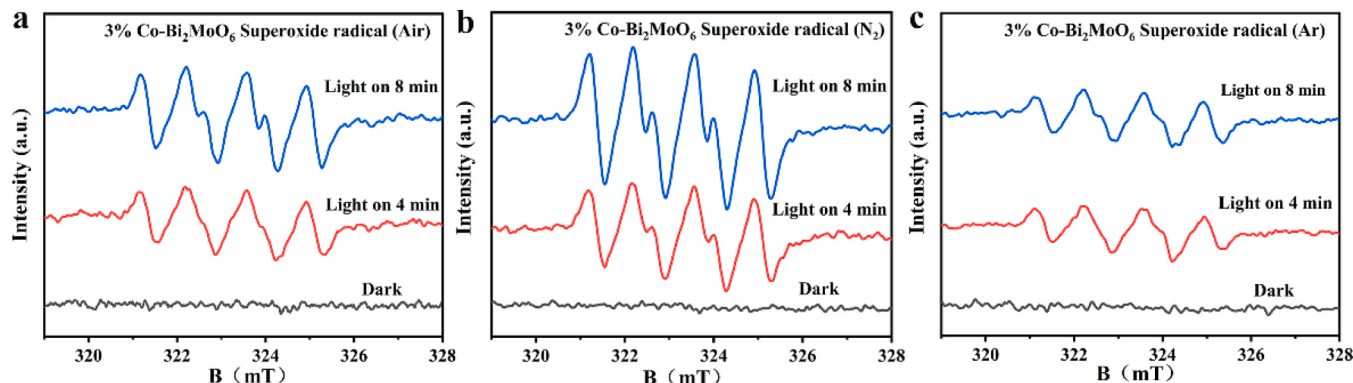


Fig. 9. DMPO spin-trapping ESR spectra of $\bullet\text{O}_2^-$ of (a) air, (b) N₂ and (c) Ar recorded with visible light irradiation of 3% Co-Bi₂MoO₆.

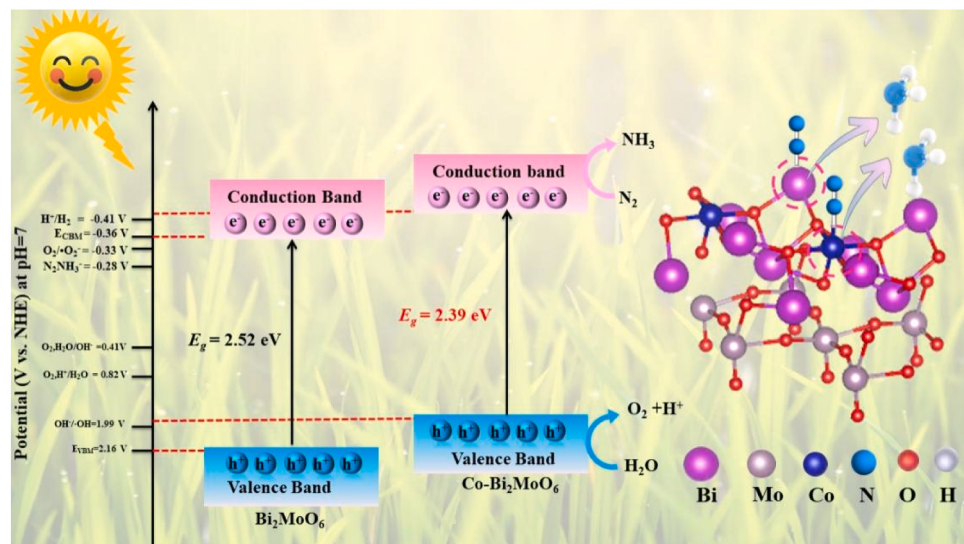


Fig. 10. Schematic of the PNRR mechanism on 3% Co-Bi₂MoO₆ with dual active sites under illumination.

curation. **Rui Du:** Investigation, Validation. **Taoxia Ma:** Investigation, Data curation. **Yujie Bian:** Review & editing. **Ruqi Li:** Validation, Review & editing. **Li Guo:** Resources, Validation, Review & editing. **Danjun Wang:** Conceptualization, Writing – review & editing, Funding acquisition. **Feng Fu:** Validation, Resources, Supervision.

Declaration of Competing Interest

The authors declare that they have no known competing financial interests or personal relationships that could have appeared to influence the work reported in this paper.

Data availability

Data will be made available on request.

Acknowledgements

This work was financially supported by the National Natural Science Foundation of China (No.22168040, 22162025) and the Project of Science & Technology Office of Shaanxi Province (No.2022JM-062).

Appendix A. Supporting information

Supplementary data associated with this article can be found in the online version at [doi:10.1016/j.apcatb.2023.123057](https://doi.org/10.1016/j.apcatb.2023.123057).

References

- [1] J.A. Pool, E. Lobkovsky, P.J. Chirik, Hydrogenation and cleavage of dinitrogen to ammonia with a zirconium complex, *Nature* 427 (2004) 527–530.
- [2] Y. Dong, T. Wang, S. Hu, Y. Tang, X. Hu, Y. Ye, H. Li, D. Cao, Electrochemical reduction of N₂ into NH₃ under ambient conditions using Ag-doped TiO₂ Nanofibers, *ACS Appl. Nano Mater.* 4 (2021) 10370–10377.
- [3] G. Jiang, Z. Li, L. Mou, S. He, Dual iron sites in activation of N₂ by iron-sulfur cluster anions Fe₅S₂ and Fe₅S₃, *J. Phys. Chem. Lett.* 12 (2021) 9269–9274.
- [4] W. Zhang, Y. Shen, F. Pang, D. Quek, W. Niu, W. Wang, P. Chen, Facet-dependent catalytic performance of Au nanocrystals for electrochemical nitrogen reduction, *ACS Appl. Mater. Interfaces* 12 (2020) 41613–41619.
- [5] S. Wang, F. Ichihara, H. Pang, H. Chen, J. Ye, Nitrogen fixation reaction derived from nanostructured catalytic materials, *Adv. Funct. Mater.* 28 (2018), 1803309.
- [6] X. Chen, N. Li, Z. Kong, W. Ong, X. Zhao, Photocatalytic fixation of nitrogen to ammonia: state-of-the-art advancements and future prospects, *Mater. Horiz.* 5 (2018) 9–27.
- [7] C. Lv, Y. Qian, C. Yan, Y. Ding, Y. Liu, G. Chen, G. Yu, Defect engineering metal-free polymeric carbon nitride electrocatalyst for effective nitrogen fixation under ambient conditions, *Angew. Chem.* 130 (2018) 10403–10407.
- [8] R. Guan, D. Wang, Y. Zhang, C. Liu, W. Xu, J. Wang, Z. Zhao, M. Feng, Q. Shang, Z. Sun, Enhanced photocatalytic N₂ fixation via defective and fluoride modified TiO₂ surface, *Appl. Catal. B: Environ.* 282 (2021), 119580.
- [9] C. Hu, X. Chen, J. Jin, Y. Han, S. Chen, H. Ju, J. Cai, Y. Qiu, C. Gao, C. Wang, Surface plasmon enabling nitrogen fixation in pure water through a dissociative mechanism under mild conditions, *J. Am. Chem. Soc.* 141 (2019) 7807–7814.
- [10] G. Zhang, C.D. Sewell, P. Zhang, H. Mi, Z. Lin, Nanostructured photocatalysts for nitrogen fixation, *Nano Energy* 71 (2020), 104645.
- [11] Y. Fu, Y. Liao, P. Li, H. Li, S. Jiang, H. Huang, W. Sun, T. Li, H. Yu, K. Li, Layer structured materials for ambient nitrogen fixation, *Coord. Chem. Rev.* 460 (2022), 214468.

- [12] B. Sun, S. Lu, Y. Qian, X. Zhang, J. Tian, Recent progress in research and design concepts for the characterization, testing, and photocatalysts for nitrogen reduction reaction, *Carbon Energy* 5 (2023), e305.
- [13] Y. Bo, H. Wang, Y. Lin, T. Yang, R. Ye, Y. Li, C. Hu, P. Du, Y. Hu, Z. Liu, Altering hydrogenation pathways in photocatalytic nitrogen fixation by tuning local electronic structure of oxygen vacancy with dopant, *Angew. Chem. Int. Ed.* 60 (2021) 16085–16092.
- [14] N. Zhang, A. Jalil, D. Wu, S. Chen, Y. Liu, C. Gao, W. Ye, Z. Qi, H. Ju, C. Wang, X. Wu, L. Song, J. Zhu, Y. Xiong, Refining defect states in $W_{18}O_{49}$ by Mo doping: a strategy for tuning N_2 activation towards solar-driven nitrogen fixation, *J. Am. Chem. Soc.* 140 (2018) 9434–9443.
- [15] X. Chen, X. Zhang, Y. Li, M. Qi, J. Li, Z. Tang, Z. Zhou, Y. Xu, Transition metal doping BiOBr nanosheets with oxygen vacancy and exposed {102} facets for visible light nitrogen fixation, *Appl. Catal. B: Environ.* 281 (2021), 119516.
- [16] B. Hu, B. Wang, Z. Bai, L. Chen, J. Guo, S. Shen, T. Xie, C. Au, L. Jiang, S. Yin, Regulating MoS_2 edge site for photocatalytic nitrogen fixation: a theoretical and experimental study, *Chem. Eng. J.* 442 (2022), 136211.
- [17] K. Li, W. Cai, Z. Zhang, H. Xie, Q. Zhong, H. Qu, Boron doped C_3N_5 for photocatalytic nitrogen fixation to ammonia: the key role of boron in nitrogen activation and mechanism, *Chem. Eng. J.* 435 (2022), 135017.
- [18] H. Yu, L. Jiang, H. Wang, B. Huang, X. Yuan, J. Huang, J. Zhang, G. Zeng, Modulation of Bi_2MoO_6 -based materials for photocatalytic water splitting and environmental application: a critical review, *Small* 15 (2019), 1901008.
- [19] X. Liu, S. Gu, Y. Zhao, G. Zhou, W. Li, BiVO₄, Bi_2WO_6 and Bi_2MoO_6 photocatalysis: a brief review, *J. Mater. Sci. Technol.* 56 (2020) 45–68.
- [20] X. Yang, X. Xu, J. Wang, T. Chen, S. Wang, X. Ding, H. Chen, Insights into the surface/interface modifications of Bi_2MoO_6 : feasible strategies and photocatalytic applications, *Sol. RRL* 5 (2021), 2000442.
- [21] Y. Zhang, L. Guo, Y. Wang, T. Wang, T. Ma, Z. Zhang, D. Wang, B. Xu, F. Fu, In-situ anion exchange based $Bi_2S_3/OV-Bi_2MoO_6$ heterostructure for efficient ammonia production: a synchronized approach to strengthen NRR and OER reactions, *J. Mater. Sci. Technol.* 110 (2022) 152–160.
- [22] V.G. Pershina, Electronic structure and properties of the transactinides and their compounds, *Chem. Rev.* 96 (1996) 1977–2010.
- [23] T. Liu, G. Tan, C. Zhao, C. Xu, Y. Su, Y. Wang, H. Ren, A. Xia, D. Shao, S. Yan, Enhanced photocatalytic mechanism of the Nd-Er co-doped tetragonal BiVO₄ photocatalysts, *Appl. Catal. B: Environ.* 213 (2017) 87–96.
- [24] F. Xu, K. Meng, S. Cao, C. Jiang, T. Chen, J. Xu, J. Yu, Step-by-step mechanism insights into the TiO_2/Ce_2S_3 S-scheme photocatalyst for enhanced aniline production with water as a proton source, *ACS Catal.* 12 (2021) 164–172.
- [25] D.K. Yesudoss, H. Chun, B. Han, S. Shammugam, Accelerated N_2 reduction kinetics in hybrid interfaces of $NbTiO_4$ and nitrogen-doped carbon nanorod via synergistic electronic coupling effect, *Appl. Catal. B: Environ.* 304 (2022), 120938.
- [26] W. Guo, K. Zhang, Z. Liang, R. Zou, Q. Xu, Electrochemical nitrogen fixation and utilization: theories, advanced catalyst materials and system design, *Chem. Soc. Rev.* 48 (2019) 5658–5716.
- [27] S. Chen, D. Liu, T. Peng, Fundamentals and recent progress of photocatalytic nitrogen-fixation reaction over semiconductors, *Sol. RRL* 5 (2021), 2000487.
- [28] J. Zhao, Z. Chen, Single Mo atom supported on defective boron nitride monolayer as an efficient electrocatalyst for nitrogen fixation: a computational study, *J. Am. Chem. Soc.* 139 (2017) 12480–12487.
- [29] J. Cao, J. Li, W. Chu, W. Cen, Facile synthesis of Mn-doped BiOCl for metronidazole photodegradation: optimization, degradation pathway, and mechanism, *Chem. Eng. J.* 400 (2020), 125813.
- [30] C. Wang, Y. Zhang, W. Wang, D. Pei, G. Huang, J. Chen, X. Zhang, H. Yu, Enhanced photocatalytic degradation of bisphenol A by Co-doped BiOCl nanosheets under visible light irradiation, *Appl. Catal. B: Environ.* 221 (2018) 320–328.
- [31] Z. Sun, X. Yang, X. Yu, L. Xia, Y. Peng, Z. Li, Y. Zhang, J. Cheng, K. Zhang, J. Yu, Surface oxygen vacancies of Pd/Bi_2MoO_{6-x} acts as "Electron Bridge" to promote photocatalytic selective oxidation of alcohol, *Appl. Catal. B: Environ.* 285 (2021), 119790.
- [32] G. Di, Z. Zhu, H. Zhang, Y. Qiu, D. Yin, J. Crittenden, Simultaneous sulfamethazine oxidation and bromate reduction by Pd-mediated Z-scheme $Bi_2MoO_6/g-C_3N_4$ photocatalysts: Synergistic mechanism and degradative pathway, *Chem. Eng. J.* 401 (2020), 126061.
- [33] K. Jing, W. Ma, Y. Ren, J. Xiong, B. Guo, Y. Song, S. Liang, L. Wu, Hierarchical Bi_2MoO_6 spheres in situ assembled by monolayer nanosheets toward photocatalytic selective oxidation of benzyl alcohol, *Appl. Catal. B: Environ.* 243 (2019) 10–18.
- [34] G. Zhang, D. Chen, N. Li, Q. Xu, H. Li, J. He, J. Lu, Fabrication of Bi_2MoO_6/ZnO hierarchical heterostructures with enhanced visible-light photocatalytic activity, *Appl. Catal. B: Environ.* 250 (2019) 313–324.
- [35] J. Tang, Y. Ge, J. Shen, M. Ye, Facile synthesis of $CuCo_2S_4$ as a novel electrode material for ultrahigh supercapacitor performance, *Chem. Commun.* 52 (2016) 1509–1512.
- [36] Q. Meng, C. Lv, J. Sun, W. Hong, W. Xing, L. Qiang, G. Chen, X. Jin, High-efficiency Fe-Mediated Bi_2MoO_6 nitrogen-fixing photocatalyst: Reduced surface work function and ameliorated surface reaction, *Appl. Catal. B: Environ.* 256 (2019), 117781.
- [37] X. Li, H. Shi, S. Zuo, B. Gao, C. Han, T. Wang, C. Yao, C. Ni, Lattice reconstruction of one-dimensional mineral to achieve dendritic heterojunction for cost-effective nitrogen photofixation, *Chem. Eng. J.* 414 (2021), 128797.
- [38] Y. Xin, S. Wang, H. Yuan, T. Hou, W. Zhu, Y. Liu, Y. Yao, W. Zhang, S. Liang, L. Wang, Atomic-level insights into the activation of nitrogen via hydrogen-bond interaction toward nitrogen photofixation, *Chem* 7 (2021) 2118–2136.
- [39] T. Wang, J. Liu, P. Wu, C. Feng, D. Wang, H. Hu, G. Xue, Direct utilization of air and water as feedstocks in the photo-driven nitrogen reduction reaction over a ternary Z-scheme $Si_9Co_3/PDA/BWO$ hetero-junction, *J. Mater. Chem. A* 8 (2020) 16590–16598.
- [40] T. Wang, C. Feng, J. Liu, D. Wang, H. Hu, J. Hu, Z. Chen, G. Xue, Bi_2WO_6 hollow microspheres with high specific surface area and oxygen vacancies for efficient photocatalysis N_2 fixation, *Chem. Eng. J.* 414 (2021), 128827.
- [41] X. Sun, D. Jiang, L. Zhang, S.M. Sun, W.Z. Wang, Enhanced nitrogen photofixation over $LaFeO_3$ via acid treatment, *ACS Sustain. Chem. Eng.* 5 (2017) 9965–9971.
- [42] X. Gao, L. An, D. Qu, W. Jiang, Y. Chai, S. Sun, X. Liu, Z. Sun, Enhanced photocatalytic N_2 fixation by promoting N_2 adsorption with a co-catalyst, *Sci. Bull.* 64 (2019) 918–925.
- [43] J. Yang, Y. Guo, R. Jiang, F. Qin, H. Zhang, W. Lu, J. Wang, J. Yu, High-efficiency "working-in-tandem" nitrogen photofixation achieved by assembling plasmonic gold nanocrystals on ultrathin titania nanosheets, *J. Am. Chem. Soc.* 140 (2018) 8497–8508.
- [44] S. Gao, R. Wu, M. Sun, M. Guo, D.B. DuBois, S. Chen, H. Ji, C. Wang, Q. Wang, High-performance nitrogen photofixation by $Bi_2Sn_2O_7$ nanoparticles enriched with oxygen vacancies, *Appl. Catal. B: Environ.* 324 (2023), 122260.
- [45] P. Li, Z. Zhou, Q. Wang, M. Guo, S. Chen, J. Low, R. Long, W. Liu, P. Ding, Y. Wu, Visible-light-driven nitrogen fixation catalyzed by Bi_5O_7Br nanostructures: enhanced performance by oxygen vacancies, *J. Am. Chem. Soc.* 142 (2020) 12430–12439.
- [46] X. Liu, Y. Luo, C. Ling, Y. Shi, G. Zhan, H. Li, H. Gu, K. Wei, F. Guo, Z. Ai, Rare earth La single atoms supported MoO_{3-x} for efficient photocatalytic nitrogen fixation, *Appl. Catal. B: Environ.* 301 (2022), 120766.